JOURNAL OF GUIDANCE, CONTROL, AND DYNAMICS
Vol. 32, No. 6, November–December 2009

Energetics of Control Moment Gyroscopes as Joint Actuators

Daniel Brown* and Mason Peck†
Cornell University, Ithaca, New York 14850

DOI: 10.2514/1.42313

This work compares the power and energy used by a robotic linkage actuated by either joint motors or scissored pairs of control moment gyroscopes. The objectives are to establish straightforward sizing equations that provide a basis for deciding on a system architecture and to validate them with detailed models. The resulting parallels between joint motor and control moment gyroscope actuation increase intuition for and inform the design of control moment gyroscopes on a single-body satellite. Control moment gyroscopes are chosen as an energy-efficient means of reactionless actuation that reduce nonlinearities and coupling between the robot and the spacecraft attitude control system. Scissored-pair control moment gyroscopes are well suited for robotics applications because the output torque acts only along the joint axis, eliminating undesirable gyroscopic reaction torques. Both analysis and simulation of a single-link robot demonstrate that the control moment gyroscope power is equal to the equivalent joint motor power for a large range of gimbal inertias and maximum gimbal angles. The transverse rate of the link does not affect this result. A two-link robot with orthogonal joint axes gives results similar to the single-link system unless momentum is not conserved about the joint. For a two-link robot with parallel joint axes, control moment gyroscopes outperform joint motors in power required when the joints rotate with opposite sign; the reverse is true when the joints act in unison. These surprising differences arise because control moment gyroscopes produce body torques with a zero-torque boundary condition at the joint, whereas joint motors produce torques that are reacted onto two adjacent links. The analysis concludes with pros and cons of control moment gyroscopes as robotic joint actuators.

Nomenclature

B	=	body fixed
G	=	gimbal fixed
N	=	Newtonian (inertial)
R	=	rotor fixed
$\dot{x}$	=	time derivative of the scalar x
$\overset{Y}{\boldsymbol{x}}$	=	time derivative of the vector $\boldsymbol{x}$ taken in frame Y, $({}^{Y}\mathrm{d}/\mathrm{d}t)(\boldsymbol{x})$

Vectors

$\boldsymbol{a}_i$	=	inertial acceleration of the ith link's center of mass
$\hat{\boldsymbol{g}}$	=	direction of the gimbal axis
$\boldsymbol{H}_x$	=	angular momentum of body x, including actuator momentum when applicable, about its center of mass or its joint axis if so indicated
$\hat{\boldsymbol{h}}$	=	direction of rotor's spin axis
$\boldsymbol{h}_r$	=	rotor angular momentum measured relative to the gimbal frame, $\boldsymbol{I}_r \cdot \boldsymbol{\omega}^{R/G}$
$\hat{\boldsymbol{n}}$	=	unit vector normal to $\hat{\boldsymbol{t}}$ and $\hat{\boldsymbol{g}}$
$\boldsymbol{R}_i$	=	inertial location of the ith link's center of mass
$\boldsymbol{r}_i$	=	body-fixed location of the ith link's center of mass
$\hat{\boldsymbol{t}}$	=	direction of desired output torque, along the joint axis for revolute joints
$\boldsymbol{v}_i$	=	inertial velocity of the ith link's center of mass
$\boldsymbol{\tau}_{\mathrm{cmg}}$	=	torque reacted onto a body by a control moment gyroscope or a scissored pair of control moment gyroscopes
$\boldsymbol{\omega}^{X/Y}$	=	angular velocity of frame X with respect to frame Y

Dyadics

$\boldsymbol{I}_x$	=	inertia of body x about its center of mass, including actuator inertia when applicable
$\mathbf{1}$	=	unit dyadic

Scalars

E	=	energy
h_r	=	magnitude of the approximate rotor angular momentum, $\boldsymbol{h}_r \cdot \hat{\boldsymbol{h}}$
I_x	=	inertia of body or component x about $\hat{\boldsymbol{h}}$ axis; about the joint axis or spherical if not indicated
k_{OA}	=	output-axis stiffness
n	=	number of links in the robot not including the base
P	=	power
θ	=	joint angle
ϕ	=	gimbal angle

Subscripts

b	=	body or link
c	=	control-moment gyroscope-driven robot link (when a distinction is required, as for $\boldsymbol{H}_c$ vs $\boldsymbol{H}_{\mathrm{cmg}}$)
cmg	=	control moment gyroscope
g	=	gimbal
i, k, m	=	indexing variables
j	=	joint motor
r	=	rotor
rel	=	relative to joint-torque-actuated robot, as in $P_{\mathrm{rel}} = P_{\mathrm{cmg}}/P_j$
sp	=	scissored-pair control moment gyroscope

Presented as Paper 7271 at the AIAA Guidance, Navigation and Control Conference and Exhibit, Honolulu, HI, 18–21 August 2008; received 21 November 2008; revision received 9 June 2009; accepted for publication 29 June 2009.

*Graduate Student, Mechanical and Aerospace Engineering, 138 Upson Hall. Student Member AIAA.

†Assistant Professor, Mechanical and Aerospace Engineering, 212 Upson Hall. Member AIAA.

I. Introduction

CONTROL moment gyroscopes (CMGs) are a means of providing attitude control of satellites without expending propellant. Thus, they contribute to reduced launch mass and longer spacecraft life. CMGs have important flight heritage controlling

large space structures such as Skylab, the International Space Station, and Mir, all of which demand very high torques. A CMG's ability to produce large torques in a small package also has applications for smaller satellites with greater agility [1–3]. This paper discusses another emerging area of possible CMG application: robotic joint actuators. The primary motivation for this study is the prospect of using CMGs for reactionless actuation to reduce or eliminate the disturbances imparted by traditional joint motors and to reduce the associated demands on the spacecraft attitude control system [4].

The motion of a robot arm in space imparts reaction forces and torques onto the spacecraft base, resulting in nonlinear coupling between the base motion and the robot motion. These effects become more pronounced as the size of the robot increases relative to the base and as robot accelerations increase. When the coupling between the robot and base spacecraft is small, control schemes used for terrestrially based robot arms may be used (see, for example, [5,6]). Other alternative control schemes include compensating for the robot motion with the spacecraft thrusters and attitude controller [7] or path planning of both the robot and the spacecraft [8]. For a recent review of dynamics and control of free-flying robots in space, see [9].

An alternative approach is to reduce or eliminate the coupling between the spacecraft and the robot through reactionless actuation (Fig. 1). In this paper, robotic actuation that does not impart a torque about the joint axis is termed reactionless actuation. With reactionless actuation, system-level pointing accuracy can be improved by reducing the known disturbances created by a robotic arm. Furthermore, the agility required of a specific subsystem need not be applied to the satellite as a whole. Reaction wheel assemblies (RWAs), clever gear design, and CMGs are all possible reactionless actuators [10]. An RWA-driven robot, such as the one described in [11,12], can be energetically costly as compared with CMGs [11]. The work in [4] demonstrates the reduced reaction torques on the spacecraft from the robot when CMGs are used in place of direct-drive motors for joint actuation. Other relevant work in the literature includes a proposed bifocal relay telescope that uses CMG attitude control on one member and connects the other member with a joint motor [13]. CMGs have also been proposed for vibration and slew control of a large truss [14].

Although the actuator reaction torques reflected onto the spacecraft through the joint axis are eliminated with reactionless actuation, the reaction forces and torques attributable to the motion of the robot arm from D'Alembert's principle are not (F_R in Fig. 1). Mitigating vibrations from the rapidly spinning rotors adds complexity to the design of CMGs. Furthermore, reactionless actuators have much greater restrictions on the end-effector forces and torques than typical joint motors, because persistent torques will saturate both and CMGs. Therefore, the pros and cons of reactionless actuation must be weighed against the pros and cons of traditional joint actuation in choosing robot-arm architectures for specific applications.

The objective of this paper is to compare power and energy used by CMGs to joint motors asked to perform the same task. The goals include establishing straightforward sizing equations that provide a basis for deciding on a system architecture and validating them with detailed models. The equations and simulations in this work refer to the equivalent joint motor system throughout. Section II reviews the dynamics and actuation torque of individual and scissored-pair CMGs. Section III concentrates on a single-link robot, using both analysis and simulation to explore power cost for CMGs and joint motors. Section IV introduces the general equations for an n-link robot arm with CMGs. Section V uses the example of two-link robots to highlight the key differences in the equations of motion. Simulations help quantify the effects of these differences on the energy used for a given maneuver. The paper concludes with pros and cons for this approach.

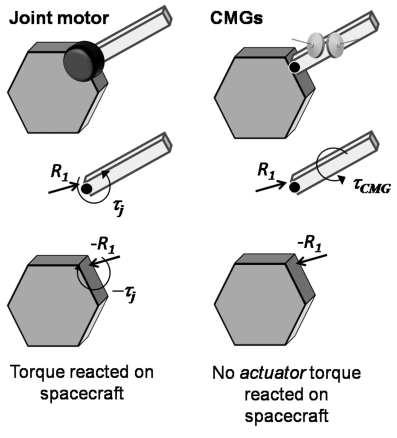

Fig. 1 Reactionless actuation with CMGs.

II. CMG Dynamics

CMGs belong to a broader class of actuators that use momentum to control the attitude or position of a body. Simply stated, a spinning body resists change in both the magnitude and the direction of spin (i.e., the change in angular momentum is equal to the applied moments). The embedded momentum of a spinning rotor mounted on a body can be used to produce an internal torque that causes the body to rotate in such a way that the system's angular momentum stays constant. A body that uses momentum to control orientation can reorient without propellant and without changing its system net angular momentum, which are valuable features in spacecraft applications. Typically, either a fixed-axis variable-speed rotor (reaction wheel) or a gimbaled-axis constant-speed rotor (CMG) or both (including variable-speed CMGs [15]) provide the momentum. Linear momentum actuators have also been considered for controlling micron-scale systems [16] but are not considered here.

An RWA governs its momentum by changing only its rotor speed. The spin axis is fixed to the satellite. The approximate energy cost of using an RWA of inertia I_r is the change in the kinetic energy of the rotor from the initial to final wheel speeds:

$$\Delta E_r = \tfrac{1}{2} I_r(\omega_2^2 - \omega_1^2) \tag{1}$$

The initial and final speeds of the rotor (ω_1, ω_2) are taken relative to an inertial reference frame. Even if RWA efficiency is improved by recovering some of the energy stored in the rotor, maximum power requirements limit the torque that may be applied by the reaction wheel. In spite of the high energy cost, reaction wheels have been used extensively due to their simplicity, reliability, and strong flight heritage. In contrast, the CMG uses a constant-speed rotor with angular momentum $\boldsymbol{h}_r$, rotated about a gimbal axis to change the angular momentum and produce a torque $\boldsymbol{\tau}_{\text{out}}$, as shown in Fig. 2. Its rotor's kinetic energy changes only insignificantly (e.g., in response to low-speed base motions). A CMG does use at least as much energy as the change in the satellite body's kinetic energy, but still much less than would be used by an RWA. Comparisons of RWAs and CMGs have previously shown the power benefits of using CMGs over RWAs, both in attitude control [1,17] and specifically for robotic applications [11]; the former references tested physical systems and the latter reference compares simulation results. This paper is the first comparison of CMGs with joint motors for robotic applications. In this work, as well as in the simulations reported in [11], the startup and standby power of CMGs are not considered. This observation does not invalidate previous comparisons with reaction wheels that must also operate at a nominal speed to avoid zero crossings, but it does indicate that the joint motor system has a key advantage over CMGs of drawing near-zero power in a quiescent state.

A. Single CMG

This section develops the equations of motion for a single CMG to obtain an expression for the gimbal torque. The gimbal torque is combined with gimbal velocity in later sections to determine power used by the CMGs. Similar equations have been developed elsewhere [11,18], but the following first-principles derivations clarify the assumptions made in this work and help establish notation.

Consider a control moment gyro attached to a body (e.g., attached to a segment of a robot arm). The CMG's angular-momentum vector

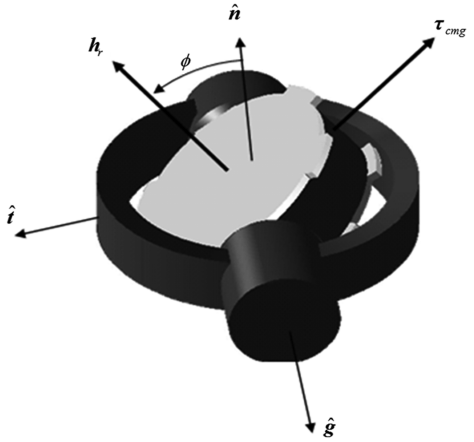

Fig. 2 CMG vectors and scalars defined.

about its center of mass, $\boldsymbol{H}_{\text{cmg}}$, is the sum of the momentum of the gimbal and the rotor:

$$\boldsymbol{H}_{\text{cmg}} = \boldsymbol{I}_g \cdot \boldsymbol{\omega}^{G/N} + \boldsymbol{I}_r \cdot \boldsymbol{\omega}^{R/N} = \boldsymbol{I}_g \cdot (\boldsymbol{\omega}^{G/B} + \boldsymbol{\omega}^{B/N}) + \boldsymbol{I}_r \cdot (\boldsymbol{\omega}^{R/G} + \boldsymbol{\omega}^{G/B} + \boldsymbol{\omega}^{B/N}) \tag{2}$$

Collecting terms and writing $\boldsymbol{I}_r \cdot \boldsymbol{\omega}^{R/G} = \boldsymbol{h}_r$ allows $\boldsymbol{H}_{\text{cmg}}$ to be expressed as

$$\boldsymbol{H}_{\text{cmg}} = \boldsymbol{I}_{\text{cmg}} \cdot (\boldsymbol{\omega}^{G/B} + \boldsymbol{\omega}^{B/N}) + \boldsymbol{h}_r \tag{3}$$

The total CMG inertia is $\boldsymbol{I}_g + \boldsymbol{I}_r = \boldsymbol{I}_{\text{cmg}}$.

The torque produced by the CMG onto the spacecraft or robot link, $\boldsymbol{\tau}_{\text{cmg}}$, is found by taking the time derivative of Eq. (2) in the N frame:

$$\boldsymbol{\tau}_{\text{cmg}} = -\boldsymbol{H}^N_{\text{cmg}} - \boldsymbol{\tau}_g \tag{4}$$

$$\boldsymbol{H}^N_{\text{cmg}} = \boldsymbol{I}_{\text{cmg}} \cdot (\ddot{\phi}\,\hat{\boldsymbol{g}} + \overset{B}{\boldsymbol{\omega}}{}^{B/N} - \dot{\phi}\,\hat{\boldsymbol{g}} \times \boldsymbol{\omega}^{B/N}) + (\dot{\phi}\,\hat{\boldsymbol{g}} + \boldsymbol{\omega}^{B/N}) \times [\boldsymbol{I}_{\text{cmg}} \cdot (\dot{\phi}\,\hat{\boldsymbol{g}} + \boldsymbol{\omega}^{B/N}) + \boldsymbol{h}_r] \tag{5}$$

where $\boldsymbol{\omega}^{G/B} = \dot{\phi}\,\hat{\boldsymbol{g}}$. In the case of an $\boldsymbol{I}_{\text{cmg}}$ that is constant in any frame, as for a spherical body,

$$(\dot{\phi}\,\hat{\boldsymbol{g}} + \boldsymbol{\omega}^{B/N}) \times [\boldsymbol{I}_{\text{cmg}} \cdot (\dot{\phi}\,\hat{\boldsymbol{g}} + \boldsymbol{\omega}^{B/N})]$$

is eliminated from Eq. (5). A spherical CMG inertia closely approximates a physical system because $\boldsymbol{I}_{\text{cmg}}$ consists of the rotor, the gimbal support structure, and both gimbal and rotor motors. A study of high-accuracy control algorithms or a geometrical analysis of the rotor and gimbal would require an exact $\boldsymbol{I}_{\text{cmg}}$, but a power comparison between a joint-motor-actuated robot and a CMG with a spherical $\boldsymbol{I}_{\text{cmg}}$ still has value for designing more general CMGs. Furthermore, the six time-varying parameters required to describe the CMG's inertia dyadic are replaced with just one. Mathematically, the CMG inertia may be written as

$$\boldsymbol{I}_g + \boldsymbol{I}_r = \boldsymbol{I}_{\text{cmg}} = I_{\text{cmg}}\mathbf{1} \tag{6}$$

This work also assumes that the CMG rotor and gimbal are rigid bodies. However, flexible effects of the rotor and gimbal along the $\hat{\boldsymbol{g}} \times \hat{\boldsymbol{h}}$ axis increase $\boldsymbol{\tau}_g$. The CMG inertia must therefore also include the output-axis stiffness k_{OA} [19]:

$$I_{\text{cmg}} = I_g + I_r + (h_r^2/k_{\text{OA}}) \tag{7}$$

The torques acting on the CMG are the applied gimbal torque and the torque reacted onto the body. In the absence of friction, electromagnetic forces, and flexible effects, the time derivative of the CMG angular momentum equals the external torques. To first order, the torque acting on the spacecraft is given by the gimbal rate crossed with the rotor momentum, resulting in the classic expression for gyroscopic torque (see Fig. 2):

$$\boldsymbol{\tau}_{\text{cmg}} = -\dot{\phi}\,\hat{\boldsymbol{g}} \times \boldsymbol{h}_r \tag{8}$$

The torque required of the gimbal motor is

$$\tau_g = I_{\text{cmg}}\ddot{\phi} + I_{\text{cmg}}\overset{B}{\boldsymbol{\omega}}{}^{B/N} \cdot \hat{\boldsymbol{g}} + (\boldsymbol{\omega}^{B/N} \times \boldsymbol{h}_r) \cdot \hat{\boldsymbol{g}} \tag{9}$$

Even for a stationary body ($\boldsymbol{\omega}^{B/N} = 0$), Eq. (8) shows that the CMG torque on the body varies due to the changing gimbal angle.

Adapting to changing CMG output torque is among the biggest challenges of CMG-based attitude-control system design, because the array of CMGs can encounter singularities [20,21]. Singularities arise when the possible gimbal motions cannot produce the desired output torque from the array. For the system under investigation here, the desired torque is always along the robot's joint axis. A scissored pair both constrains the torque output to act only along the joint axis and avoids the internal singularities associated with more general CMG arrays.

B. Scissored Pairs

In a scissored pair of CMGs, two CMGs with parallel gimbal axes maintain equal-magnitude and opposite-sign gimbal angles (Fig. 3). Scissored pairs, also referred to as V gyros or twin gyros [22], produce torque about a single axis by using antisymmetric (equal magnitude, opposite direction) gimbal angles to cancel unwanted torque on the body. Cross-coupling torques acting on the gimbal motors that result from body motion can be canceled internally to reduce gimbal torque [22–24]. Singularities occur in a scissored pair only if the commanded torque exceeds the gimbal-rate capability of the scissored pair in magnitude or if the momentum stored in the pair is at a maximum. Related saturation singularities occur in any actuator. Scissored pairs also have a simple zero-angular-momentum configuration, useful for rotor spin-up and ensuring that motion of other robot links does not induce unwanted gyroscopic torque even though the rotors spin continuously. Although this paper does not explore the application of a single CMG for each link, there may be some benefit to be gained by using them in this way.

As shown in Fig. 3, a single gimbal motor with a mechanical coupling between CMGs is selected for the scissored-pair actuation [23]. In such a system, the torque applied to the scissored pair by the gimbal motor, τ_{sp}, is equal to the difference between the torque from each gear to the individual CMGs. Applying Eq. (9) to each of the CMGs and letting $\phi_2 = -\phi_1$, the applied torque is [23]

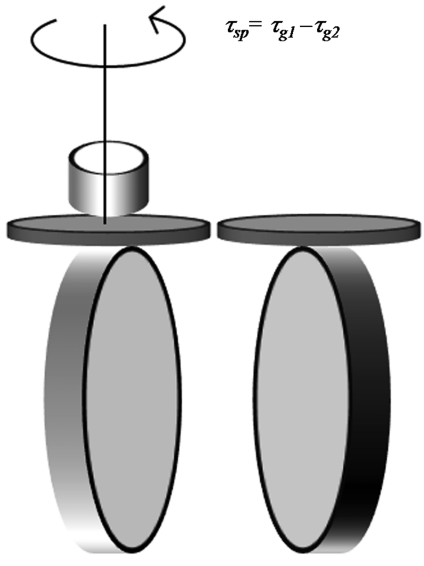

Fig. 3 Geared scissored pair.

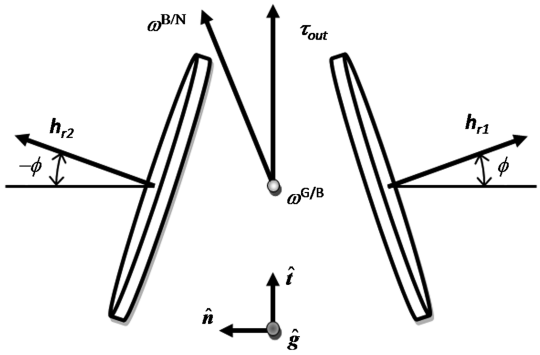

Fig. 4 Scissored-pair kinematics.

$$\tau_{\text{sp}} = \tau_{g1} - \tau_{g2} \tag{10}$$

$$\tau_{\text{sp}} = 2I_{\text{cmg}}\ddot{\phi} - \boldsymbol{\omega}^{B/N} \cdot 2h_r \cos\hat{\boldsymbol{t}} \tag{11}$$

where the unit vector $\hat{\boldsymbol{t}}$ shown in Fig. 4 defines the robot's joint axis. The dot product of the body rate and the scissored-pair angular momentum replaces a scalar triple product in Eq. (9) when a geared scissored pair is used. The torque required to accelerate just the CMG inertia is $2I_{\text{cmg}}\ddot{\phi}$. The additional contribution of $\boldsymbol{\omega}^{B/N}$ to τ_{sp} is called the base-rate effect, though the term body rate is used in this paper to avoid confusion between the robot base and the body driven by the CMGs. The body-rate effect, arising from the motion of the satellite or robot link that the CMG is attached to, plays a significant role in energy costs of CMGs. The rotor momentum is usually large relative to the gimbal inertia and accelerations, with the latter limited by the gimbal motor. A simplified expression for gimbal torque that is useful for deriving compact analytical results for building intuition is

$$\tau_{\text{sp}} \approx -\boldsymbol{\omega}^{B/N} \cdot 2h_r \cos\phi\hat{\boldsymbol{t}} \tag{12}$$

Although some of the analytical results are obtained using Eq. (12), the simulations use the complete gimbal torque from Eq. (11).

An important consequence of the body-rate effect is how it affects power usage of a CMG. It arises because the CMG consumes at least as much power as needed to move the body to which the CMG is mounted. From the work-energy principle [25], the power used by the CMGs for a maneuver is the product of gimbal torque and gimbal rate:

$$P_{\text{cmg}} = |\tau_{\text{sp}}\dot{\phi}| \tag{13}$$

This expression neglects electromagnetic inefficiencies under the likely assumption that the gimbal torque per se drives the power design in an agile application. Friction losses may make CMGs an inefficient choice for a generally quiescent system. The absolute value in Eq. (13) means that power is independent of the sign of gimbal torque and gimbal rate. This study does not distinguish between positive or negative power because both require work from the gimbal motor. The sign would matter in a case in which the spacecraft power system efficiently recovered this energy expenditure in a regenerative fashion (e.g., using the gimbal motor as a generator). In practice, such an approach may not be very efficient, or it may be too costly and complex. Such an architecture is not in place for the purposes of this study. Therefore, these comparisons consider only the absolute value of power.

III. Single-Link Robot Arm

This section analyzes actuation of a single-link robot as a single-degree-of-freedom system to obtain an analytical expression for power used by either a joint motor between the spacecraft and robot or a scissored pair of CMGs on the robot. The cost of additional attitude control effort when using a joint motor is not included. The differences in actuator mass are also not included. Although important trades can be made between actuator mass and system mass and performance, this paper focuses on the contribution of CMGs as joint actuators. Equal actuator mass and inertia also establishes an equivalent system in which the CMGs are conceptually replaced with joint torques to analyze the tradeoffs associated with sizing CMGs in this or any CMG-driven system in terms of an equivalent system driven by joint motors.

A. Single-Link Analysis

The dynamics of a single-link robot with a joint motor are given first as the reference system and are then augmented to obtain the dynamics of the CMG-driven system.

1. *Joint-Torque-Driven Robot*

Suppose the robot link's angular momentum about the joint axis is

$$\boldsymbol{H}_b = \boldsymbol{H}_j = \boldsymbol{I}_b \cdot \boldsymbol{\omega}^{B/N} \tag{14}$$

Because $\boldsymbol{v}_j$, the velocity of the center of mass, is not explicitly included in $\boldsymbol{H}_b$, $\boldsymbol{I}_b$ is the inertia of the link (including actuator inertia) measured about either the center of mass or an inertially fixed point, whichever intersects the joint axis $\hat{\boldsymbol{t}}$. The link's inertial angular velocity $\boldsymbol{\omega}^{B/N}$ need not be parallel to the joint axis. The angular momentum derivative is

$$\overset{N}{\boldsymbol{H}}_b = \boldsymbol{I}_b \cdot \overset{B}{\boldsymbol{\omega}}^{B/N} + \boldsymbol{\omega}^{B/N} \times (\boldsymbol{I}_b \cdot \boldsymbol{\omega}^{B/N}) \tag{15}$$

The joint torque acting about $\hat{\boldsymbol{t}}$ is given by

$$\tau_j = \boldsymbol{I}_b \cdot \overset{B}{\boldsymbol{\omega}}^{B/N} \cdot \hat{\boldsymbol{t}} + (\boldsymbol{\omega}^{B/N} \times (\boldsymbol{I}_b \cdot \boldsymbol{\omega}^{B/N})) \cdot \hat{\boldsymbol{t}} \tag{16}$$

2. *CMG-Driven Robot*

Including the actuator inertia in $\boldsymbol{I}_b$ for comparing CMGs and joint motors separates the obvious effects on power of increasing inertia from the remaining gyroscopic effects of the CMGs. The angular momentum of the CMG-driven system is the same $\boldsymbol{H}_b$ as for the joint-driven robot with the additional angular momentum due to the CMGs:

$$\begin{aligned}\boldsymbol{H}_c = \boldsymbol{H}_b + \boldsymbol{h}_{\text{cmg1}} + \boldsymbol{h}_{\text{cmg2}}\boldsymbol{H}_c = \boldsymbol{I}_b \cdot \boldsymbol{\omega}^{B/N} + \boldsymbol{I}_{\text{cmg1}} \cdot \boldsymbol{\omega}^{G1/B} \\ + \boldsymbol{h}_{r1} + \boldsymbol{I}_{\text{cmg2}} \cdot \boldsymbol{\omega}^{G2/B} + \boldsymbol{h}_{r2}\end{aligned} \tag{17}$$

For the scissored-pair CMGs with $\boldsymbol{I}_{\text{cmg1}} = \boldsymbol{I}_{\text{cmg2}}$, the angular momentum of the gimbals cancels: that is,

$$\boldsymbol{I}_{\text{cmg1}} \cdot \boldsymbol{\omega}^{G1/B} + \boldsymbol{I}_{\text{cmg2}} \cdot \boldsymbol{\omega}^{G2/B} = 0$$

As indicated in Fig. 4, the sum of the rotor momenta becomes

$$\boldsymbol{h}_{r1} + \boldsymbol{h}_{r2} = 2h_r \sin\phi\hat{\boldsymbol{t}} \tag{18}$$

With this substitution, $\boldsymbol{H}_c$ reduces to

$$\boldsymbol{H}_c = \boldsymbol{I}_b \cdot \boldsymbol{\omega}^{B/N} + 2h_r \sin\phi\hat{\boldsymbol{t}} \tag{19}$$

The only difference between $\boldsymbol{H}_j$ and $\boldsymbol{H}_c$ is $2h_r \sin\phi\hat{\boldsymbol{t}}$. The derivative of $\boldsymbol{H}_c$ is

$$\begin{aligned}\overset{N}{\boldsymbol{H}}_c = \boldsymbol{I}_b \cdot \overset{B}{\boldsymbol{\omega}}^{B/N} + \boldsymbol{\omega}^{B/N} \times (\boldsymbol{I}_b \cdot \boldsymbol{\omega}^{B/N}) + 2h_r\dot{\phi}\cos\phi\hat{\boldsymbol{t}} \\ + \boldsymbol{\omega}^{B/N} \times 2h_r \sin\phi\hat{\boldsymbol{t}}\end{aligned} \tag{20}$$

For the CMG-driven robot, the robot freely rotates about $\hat{\boldsymbol{t}}$. Therefore, the projection of Eq. (20) onto $\hat{\boldsymbol{t}}$ must be zero:

$$0 = \boldsymbol{I}_b \cdot \overset{B}{\boldsymbol{\omega}}^{B/N} \cdot \hat{\boldsymbol{t}} + (\boldsymbol{\omega}^{B/N} \times (\boldsymbol{I}_b \cdot \boldsymbol{\omega}^{B/N})) \cdot \hat{\boldsymbol{t}} + 2h_r\dot{\phi}\cos\phi \tag{21}$$

Substituting Eq. (16) leads to an expression for the gimbal rate:

$$\dot{\phi} = \frac{-\tau_j}{2h_r \cos\phi} \tag{22}$$

This equation states that the gimbal velocity becomes infinite as the gimbal angle approaches 90 deg. Also note that gimbal velocity roughly tracks the robot acceleration due to the relationship between τ_j and $\ddot{\theta}$.

3. Joint Motor and CMG Power

Calculating power requires both torque and velocity about the axis of interest: either the joint axis or the gimbal axis. The scalar value of the angular velocity of the link about the joint axis is

$$\boldsymbol{\omega}^{B/N} \cdot \hat{\boldsymbol{t}} = \dot{\theta} \tag{23}$$

The joint motor power is

$$P_j = |\tau_j \dot{\theta}| \tag{24}$$

The CMG power is the product of the torque in Eq. (11) and the gimbal rate in Eq. (22):

$$P_{\text{cmg}} = \left| (2I_{\text{cmg}}\ddot{\phi} - 2\dot{\theta}h_r \cos\phi) \frac{-\tau_j}{2h_r \cos\phi} \right| \tag{25}$$

When $I_{\text{cmg}}\ddot{\phi}$ is small, the CMG power equals the joint motor power:

$$P_{\text{cmg}} \approx |\tau_j \dot{\theta}| \tag{26}$$

Both ϕ and h_r are eliminated when Eq. (25) is able to be reduced to Eq. (26). A gimbal angle offset, equivalent to a non-zero-momentum set point, does not affect the power usage. Likewise, misalignment of the scissored pair introduces a momentum bias perpendicular to the joint axis and serves only to reduce the available angular momentum from the scissored pair without affecting power. In conclusion, this section provides a simple derivation of the power cost for CMGs and joint motors showing that both are equal for small $I_{\text{cmg}}\ddot{\phi}$.

B. Sizing CMGs in a Scissored Pair

Because the CMG power cost (excluding baseline losses) is identical to joint motor power, CMG design principles for gimbal motor torque and speed can be expressed in terms of the same robot link parameters that are used to determine joint motor sizing. These design principals are derived for specific cases of CMG-robot configurations; the following section establishes the validity of these principals for the more general equations derived previously. In both the analysis and simulation, these design principles are valid only if the gimbal angle is limited to avoid saturating the system. With scissored pairs, the gimbal angle could acquire some bias during a rest-to-rest maneuver if the angular momentum about the joint axis is not conserved. Conservation of momentum about the joint axis $\hat{\boldsymbol{t}}$ determines the maximum gimbal angle $\phi_{\max}$ based on the maximum momentum needed by the robot arm. The necessary conditions for conservation of momentum about a joint provide a relationship between CMG momentum and link momentum that may be used to properly size the CMGs.

The change in $\boldsymbol{H}_c$ about $\hat{\boldsymbol{t}}$ is

$$\frac{\mathrm{d}}{\mathrm{d}t}(\boldsymbol{H}_c \cdot \hat{\boldsymbol{t}}) = \frac{\mathrm{d}}{\mathrm{d}t}(\boldsymbol{H}_c) \cdot \hat{\boldsymbol{t}} + \boldsymbol{H}_c \cdot \frac{\mathrm{d}}{\mathrm{d}t}(\hat{\boldsymbol{t}}) \tag{27}$$

The derivatives may be taken in any reference frame because this is a scalar equation. The first term on the right is equal to the torque about $\hat{\boldsymbol{t}}$ and is zero for a CMG-driven system. Substituting Eq. (19) for $\boldsymbol{H}_c$ and noting that the derivative of $\hat{\boldsymbol{t}}$ in the inertial frame is $\boldsymbol{\omega}^{B/N} \times \hat{\boldsymbol{t}}$ leads to

$$\frac{\mathrm{d}}{\mathrm{d}t}(\boldsymbol{H}_c \cdot \hat{\boldsymbol{t}}) = (\boldsymbol{I}_b \cdot \boldsymbol{\omega}^{B/N} + 2h_r \sin\phi \hat{\boldsymbol{t}}) \cdot (\boldsymbol{\omega}^{B/N} \times \hat{\boldsymbol{t}}) \tag{28}$$

Rearranging terms, this equation is zero if

$$[\boldsymbol{\omega}^{B/N} \times (\boldsymbol{I}_b \cdot \boldsymbol{\omega}^{B/N})] \cdot \hat{\boldsymbol{t}} = 0 \tag{29}$$

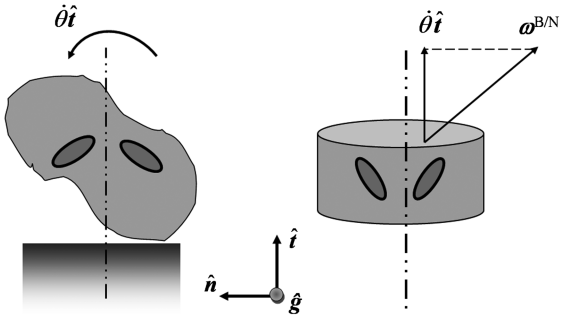

Fig. 5 Systems that conserve angular momentum about the joint axis.

Momentum about the joint axis is conserved for the two cases illustrated in Fig. 5: either the link rotates purely about the joint axis or, for arbitrary rotation of the link, the link inertia is symmetric about $\hat{\boldsymbol{t}}$.

If the condition in Eq. (29) is satisfied, then a robotic system that starts at $\boldsymbol{H}_c = 0$ and $\phi = 0$ will always satisfy $\boldsymbol{H}_c \cdot \hat{\boldsymbol{t}} = 0$. From Eq. (19), $\boldsymbol{H}_c \cdot \hat{\boldsymbol{t}}$ is

$$\boldsymbol{H}_c \cdot \hat{\boldsymbol{t}} = I_{b,\hat{t}}\dot{\theta} + 2h_r \sin\phi = 0 \tag{30}$$

The joint torque from Eq. (16) reduces to

$$\tau_j = I_{b,\hat{t}}\ddot{\theta} \tag{31}$$

Both Eqs. (30) and (31) depend on only $I_{b,\hat{t}}$ as a consequence of Eq. (29), a fact verified by considering both cases shown in Fig. 5. Combining Eq. (22) with Eq. (30) provides a bound on the gimbal rate for the one-degree-of-freedom robot:

$$|\dot{\phi}| < \ddot{\theta}_{\max} \tan(\phi_{\max})/\dot{\theta}_{\max} \tag{32}$$

This bound is conservative because the angular acceleration goes to zero when the angular velocity reaches maximum values. The bound on $|\dot{\phi}|$ also illustrates a tradeoff between designing for a high $\phi_{\max}$ to minimize the size and mass of the rotor versus designing for a more limited $\phi_{\max}$ to reduce $\dot{\phi}$.

1. Gimbal Torque and Torque Amplification

Single-gimbal CMGs are credited with a torque-amplification property, meaning that the output-to-input torque ratio is much greater than one:

$$\tau_{\text{cmg}}/\tau_g \gg 1 \tag{33}$$

It can be shown that torque amplification requires that [21,26]

$$\dot{\phi}/\dot{\theta} \gg 1 \tag{34}$$

For given link rate and acceleration requirements, the only way to satisfy both this condition and the bound in Eq. (32) is to artificially limit $\phi_{\max}$ by increasing $\boldsymbol{h}_r$. An alternative expression for the torque ratio that includes the acceleration of the body or link being actuated is found by recognizing that the CMG output torque must equal the joint motor torque. Taking the joint torque of the equivalent system from Eq. (31) as the output torque and the input torque of Eq. (11), the new proposed torque ratio is

$$\frac{\tau_{\text{cmg}}}{\tau_{\text{sp}}} = \frac{I_{b,\hat{t}}\ddot{\theta}}{2I_{\text{cmg}}\ddot{\phi} - 2\dot{\theta}h_r \cos\phi} \tag{35}$$

A simplified version of this equation for rapid design iterations would omit the contribution of gimbal inertia and acceleration:

$$\frac{\tau_{\text{cmg}}}{\tau_{\text{sp}}} \approx \frac{I_{b,\hat{t}}\ddot{\theta}}{-2\dot{\theta}h_r \cos\phi} \tag{36}$$

The CMGs amplify the input torque near $\phi = 0$, but the reverse occurs as ϕ approaches 90 deg, again underscoring the tradeoff between minimizing rotor size and gimbal motor size. Interestingly, systems without meaningful torque amplification remove one objection to double-gimbal CMGs (DGCMGs): the need to transfer large torques through the gimbal motors rather than bearings [21]. A DGCMG could reduce ACS volume [24], though questions remain regarding the reliability and accuracy of such a system [19].

When τ_{sp} is the limiting factor in a particular CMG-robot application, an estimate of the optimal h_r that maximizes $\dot{\theta}$ may be determined as follows. Consider a CMG robot that satisfies Eq. (19). For $\dot{\theta} = \dot{\theta}_{max}$, $\phi = \phi_{max}$, a constant, and $\ddot{\phi} = 0$, combining Eqs. (11) and (19) gives an expression for τ_{sp}:

$$\tau_{sp} = (2h_r)^2 \sin\phi \cos\phi / I_{b,\hat{t}} \tag{37}$$

The first-order optimality condition determines the ϕ that maximizes τ_{sp} for a given h_r:

$$\frac{\partial \tau_{sp}}{\partial \phi} = 0 = (2h_r)^2(\cos^2\phi - \sin^2\phi)/I_{b,\hat{t}} \tag{38}$$

The maximum value of τ_{sp} occurs when $\phi = k\pi/4$ ($k = 1, 3, 5,...$). Solving for h_r,

$$h_r = \sqrt{I_{b,\hat{t}}\tau_{sp}/2} \tag{39}$$

The corresponding $\dot{\theta}_{max}$ is found from Eq. (19) at

$$\dot{\theta}_{max} = \sqrt{2\tau_{sp}/I_{b,\hat{t}}}\sin\phi_{max} \tag{40}$$

A CMG-driven robot will, in general, present a varying inertia to its actuators, because motion of outer links affects the motion of the inner links. Therefore, the optimal h_r from Eq. (39) is selected for a particular robot configuration (e.g., fully extended to meet performance requirements for the greatest robot inertia taken about the shoulder joint). An abrupt change in $\dot{\theta}_{max}$ occurs for small inertias, because if τ_{sp} cannot provide enough torque to reach the designed ϕ_{max}, then $\phi_{max} < \pi/4$ due to the condition given in Eq. (38). An example plot of $\dot{\theta}_{max}$ vs total robot inertia about the fixed shoulder joint is given in Fig. 6 showing the optimal $\dot{\theta}_{max}$ when

$$h_r = \sqrt{I_{b,\hat{t}}\tau_{sp}/2}$$

compared with the realizable $\dot{\theta}_{max}$ when h_r is fixed over the range of inertias. If the CMG is too large for the gimbal motor, then performance is significantly less than would be predicted from conservation of angular momentum alone. The lower-performance region with small robot inertias may occur during testing of a robot link not attached to a base and with hardware omitted.

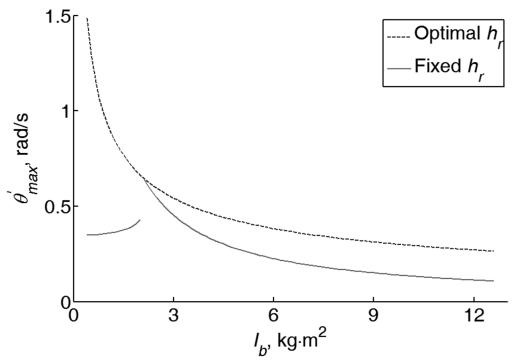

Fig. 6 Effect of inertia and τ_{sp} on $\dot{\theta}_{max}$.

2. Gimbal Acceleration

The gimbal acceleration contributes to the gimbal torque [Eq. (11)] and affects the gimbal power [Eq. (25)] and the input/output torque relationship [Eq. (35)]. Differentiating the gimbal rate in Eq. (22) in the case of angular momentum conserved about the joint axis [Eq. (29)] gives an expression for gimbal acceleration:

$$\ddot{\phi} = \frac{-I_{b,\hat{t}}\theta + 2h_r\dot{\phi}^2\sin\phi}{2h_r\cos\phi} \tag{41}$$

Two important features of the gimbal acceleration are that $\ddot{\phi} \to \infty$ as $\phi \to 90$ deg and that finite $\ddot{\phi}$ implies finite $\ddot{\theta}$. The latter conclusion implies that the jerk of the robot link will never be infinite, because infinite gimbal torque would be required.

3. Power Contributors

The factors that affect the CMG power relative to joint motor power determine how the simulation results in this paper may be scaled according to a specific set of problem parameters. A dimensionless power $\tilde{P}_{rel}$ is defined as

$$\tilde{P}_{rel} = \frac{P_{cmg} - P_j}{P_j} \tag{42}$$

When P_j is zero (e.g., at the start or end of a maneuver or when changing direction), $\tilde{P}_{rel}$ becomes unbounded. Integrating power for each system over the entire maneuver provides a more robust performance metric. Therefore, $\tilde{P}_{rel}$ by itself should not be the cost function for finding an optimal system and is used here only to determine scaling relationships.

To express $\tilde{P}_{rel}$ in terms of the design parameters of the robot, Eqs. (24) and (25) are substituted into Eq. (42):

$$\tilde{P}_{rel} = \frac{-I_{cmg}\ddot{\phi}}{\dot{\theta}h_r\cos\phi} \tag{43}$$

Substituting from Eqs. (41) and (22) eliminates $\ddot{\phi}$ and $\dot{\phi}$ from this result:

$$\tilde{P}_{rel} = \frac{I_{cmg}I_{b,\hat{t}}}{2\dot{\theta}h_r^2\cos^2\phi}\left(\theta - \frac{I_{b,\hat{t}}\ddot{\theta}^2\sin\phi}{2h_r\cos^2\phi}\right) \tag{44}$$

Relative power is a function of time. For practical use, a time-independent scaling relationship may be obtained by evaluating the maxima of $\tilde{P}_{rel}$ over all possible values of $\dot{\theta}$, $\ddot{\theta}$, $\dddot{\theta}$, and ϕ. Two obvious maxima occur as $\dot{\theta} \to 0$ or as $\phi \to \pi/2$ with a value of $\tilde{P}_{rel} \to \infty$. Therefore, a candidate local maximum of $\tilde{P}_{rel}$ would occur at ϕ_{max}, which also corresponds to $\dot{\theta} = \dot{\theta}_{max}$ and $\ddot{\theta} = 0$. However, θ may be nonzero at this instant. Therefore, Eq. (44) may take a local maximum value of

$$\tilde{P}_{rel}\Big|_{\phi=\phi_{max}} = \frac{I_{cmg}I_{b,\hat{t}}\theta_{max}}{2\dot{\theta}_{max}h_r^2\cos^2\phi_{max}} \tag{45}$$

This equation shows that the power consumption of a CMG compared with a direct-drive motor will be proportional to the product $I_{cmg}I_{b,\hat{t}}\theta_{max}$ and inversely proportional to $\dot{\theta}_{max}$ and the square of $h_r\cos\phi_{max}$.

Relative power may have another local maximum for $0 < \dot{\theta} < \dot{\theta}_{max}$, corresponding to a nonzero value of $\ddot{\theta}$. To explore the relative magnitude of $\tilde{P}_{rel}|_{\phi=\phi_{max}}$ as compared with the other local maximum, time histories of the link angle and gimbal angle from $\dot{\theta}_{max}/4 \le \dot{\theta} \le \dot{\theta}_{max}$ for values of ϕ_{max} between 55 and 80 deg are used to determine the maximum $\tilde{P}_{rel}$ in this interval, denoted as $\tilde{P}_{rel,max}$. Values of $\dot{\theta} < \dot{\theta}_{max}/4$ are likely influenced by the discontinuity in Eq. (42) at $\dot{\theta} = 0$. A plot of the relative error $(\tilde{P}_{rel,max} - \tilde{P}_{rel}|_{\phi=\phi_{max}})/\tilde{P}_{rel,max}$ in Fig. 7 shows that $\tilde{P}_{rel}|_{\phi=\phi_{max}}$ provides a reasonable

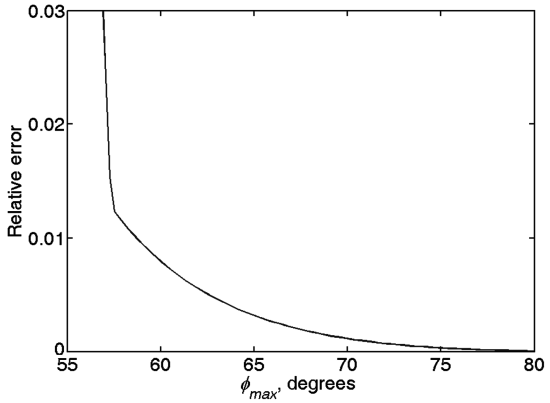

Fig. 7 Relative error $(|\tilde{P}_{\text{rel. max}} - \tilde{P}_{\text{rel}}|_{\phi=\phi_{\max}})/\tilde{P}_{\text{rel,max}}$.

approximation for $\tilde{P}_{\text{rel,max}}$ for $\dot{\theta}_{\max}/4 \le \dot{\theta} \le \dot{\theta}_{\max}$. This approximation is within 1% of $\tilde{P}_{\text{rel,max}}$ for $\phi_{\max} > 60$ deg. Another useful expression for $\tilde{P}_{\text{rel}}|_{\phi=\phi_{\max}}$ may be found by applying Eq. (30) to express $\tilde{P}_{\text{rel}}$ independently of gimbal angle:

$$\tilde{P}_{\text{rel}} = \frac{2I_{\text{cmg}} I_{b,\hat{t}} \ddot{\theta}_{\max}}{h_r^2 - (I_{b,\hat{t}} \dot{\theta}_{max})^2} \tag{46}$$

Proper sizing of CMGs involves tradeoffs between link inertia, joint velocity, rotor momentum, and gimbal angle constrained by conservation of angular momentum about the joint axis. Although the sizing and scaling relationships of this section are derived from a scissored-pair CMG array on a robot arm, they can be extended to CMG arrays used for attitude control of satellites with the generalization that the scissored-pair gimbal angle ϕ corresponds to the angle between the rotor momentum of any active CMG in an array and the output-torque axis.

C. Single-Link Simulations

As discussed previously, the local maximum relative power $\tilde{P}_{\text{rel,max}}$ gives an indication of the performance of CMGs vs joint motors. However, at the endpoints of a rest-to-rest maneuver, $\tilde{P}_{\text{rel}}$ goes to infinity as the joint rate goes to zero and does not give a good indication of the relative performance of CMGs and joint motors. This section looks more closely at the effect of CMG size as driven by gimbal inertia and maximum gimbal angle by simulating a rest-to-rest maneuver and calculating the ratio of the energy used by either CMGs or joint motors. Robot arms that do not conserve momentum about the joint axis are also simulated to explore the effect, if any, of the transverse rate of a link on CMG energy use.

1. *Trajectory Generation*

The link motions are prescribed to facilitate comparison between joint motors and scissored pairs without confounding influences from a particular control algorithm. The link is rotated through a given angle in the least amount of time that is consistent with maximum rate, acceleration, and jerk requirements. The angle profile shown in Fig. 8 reaches the maximum rate and acceleration for only an instant and is achieved via the following relationships among total link rotation and maximum rate, acceleration, and jerk:

$$\ddot{\theta}_{\max}^2 = \dddot{\theta}_{\max} \cdot \dot{\theta}_{\max} \tag{47}$$

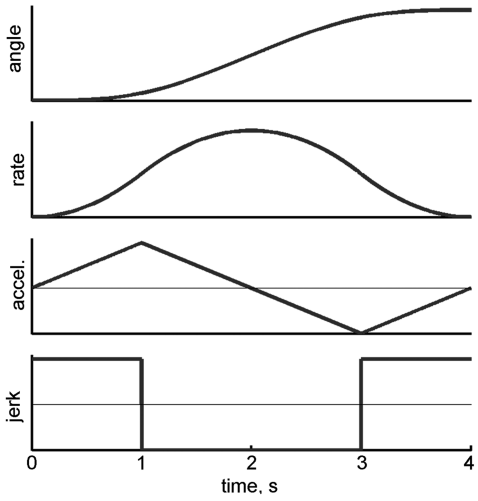

Fig. 8 Joint trajectory.

$$\Delta\theta = \dot{\theta}_{\max}\left(\frac{\dot{\theta}_{\max}}{\ddot{\theta}_{\max}} + \frac{\ddot{\theta}_{\max}}{\dddot{\theta}_{\max}}\right) \tag{48}$$

$$\Delta t = 4\ddot{\theta}_{\max}/\dddot{\theta}_{\max} \tag{49}$$

The first two relationships ensure that joint rate and acceleration reach a maximum but do not plateau during the rest-to-rest maneuver. The final relationship determines the slew time. The torque and power required by the joint motor and the scissored-pair CMGs are then calculated for the given trajectory. Integrating power over time provides the total energy used by each actuation method:

$$E_j = \int_0^T |\tau_j \dot{\theta}| \mathrm{d}t \tag{50}$$

$$E_{\text{cmg}} = \int_0^T |\tau_{\text{sp}} \dot{\phi}| \mathrm{d}t \tag{51}$$

2. *Gimbal Inertia and Maximum Gimbal Angle*

The first simulation explores the contribution of I_{cmg} and $\phi_{\max}$ to the CMG to joint motor energy ratio E_{cmg}/E_j. This simulation maintains a fixed $\boldsymbol{I}_b$ for all runs, even though I_{cmg} varies for each simulation; that is, the net link inertia $\boldsymbol{I}_b$ is identical to the $\boldsymbol{I}_b$ used for the equivalent joint motor system. This approach distinguishes the cost of increasing gimbal inertia from the cost of increasing the link inertia. The results are based on 30 evenly spaced values for $\phi_{\max}$ and I_{cmg} from 1 to 1.5 rad (57–86 deg) and 0 to 0.3 kg · m^2, respectively, as listed in Table 1. The remaining robotic-arm parameters are chosen to be unity, but they can be scaled to accommodate other designs. The rotor momentum is prescribed to conserve angular momentum about the joint axis. Figure 9 shows the energy ratio of all the simulations. The flat region in which the ratio of the energies is near unity indicates a large preferred design space for $\phi_{\max}$ and I_{cmg} such that CMGs are about as efficient as joint motors. Note that the energy ratio increases approximately linearly with both I_{cmg} and $\phi_{\max}$ in the plot, even though $\tilde{P}_{\text{rel,max}}$ is proportional to $1/\cos^2\phi$. This trend arises because E_{cmg} is the integral of P_{cmg} over the interval $0 \le \phi \le \phi_{\max}$. This simulation suggests that it is reasonable to limit $\phi_{\max}$ and I_{cmg} to about 70 deg and one-tenth of the link inertia, respectively.

Table 1 Parameters for single-link simulation

Study	$\Delta\theta$, deg	$\omega_{\max}$, s^{-1}	$a_{\max}$, s^{-2}	$j_{\max}$, s^{-3}	I_b, kg · m^2	h_r, N · m · s	$\phi_{\max}$, deg	I_{cmg}, kg · m^2	E_{cmg}/E_j
Gimbal properties	115	1	1	1	1·1	0.50–0.59	57–86	0–0.3	1.0–1.91
Body rate	115	1	1	1	0.8–1.2	0.44–0.65	60–70	0.1	1.0–1.03

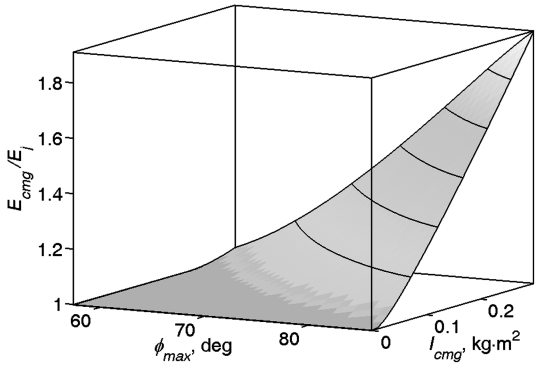

Fig. 9 Gimbal inertia and maximum gimbal angle effect on CMG energy use.

3. Transverse Rate and Arbitrary Link Inertia

CMGs are best suited for robotic systems that conserve angular momentum about the joint axis, as this avoids momentum bias that could otherwise lead to control torques that would drive the CMGs past the gimbal-angle limit. However, during the operation of a robot, such biases could easily arise in the context of payload manipulation. A robotic link may also experience such a bias if it is attached to a moving spacecraft base or other robotic links. The next simulation is of a robot arm that does not conserve momentum about its joint axis. Consider the case of a body with arbitrary inertial properties (i.e., a robot arm segment with an arbitrary payload) rotating about a transverse axis at a constant rate. Although this transverse rate is maintained through external means (e.g., spacecraft ACS or other links of the robot arm), the body of interest performs the maneuver about the body-fixed joint axis, as shown in Fig. 10. The angular velocity vector as written in the link's frame is

$$[\boldsymbol{\omega}^{B/N}]^B = [\,\omega_1 \quad \omega_2 \quad \omega_3\,]^T$$

where $\omega_1 = \dot{\theta}$ as defined in Fig. 8, and ω_2 and ω_3 are constants such that total transverse rate $\omega_0 = \sqrt{\omega_2^2 + \omega_3^2}$ is less than 1 rad/s (Fig. 10).

The link inertia varies between trials by choosing physically realizable principal moments of inertia from the range given in Table 1 and arbitrarily rotating the resulting inertia matrix to introduce offdiagonal terms in the body-fixed reference frame (i.e., the joint axis is not one of the principal axes of inertia). The offdiagonal terms ensure that the offaxis rotation contributes to the dynamics [cf. Equation (29)]. In a physically realizable inertia, the maximum principal inertia cannot be greater than the sum of the other two principal inertias. The inertia matrix must also be symmetric. Peck [27] describes a method of simulating a distribution of random inertia matrices that selects the principal inertias and randomly rotates this diagonal matrix. In this work, the principal inertias are drawn from the sum of uniform distributions, both for ease of use and to limit bias that could arise if the inertia were fixed to some arbitrary value. Physical but random and asymmetric inertia matrices further explore the effects of transverse rate on power and energy use but are not central to its conclusion. The variation of the inertia matrix also effectively accounts for a displaced mass center.

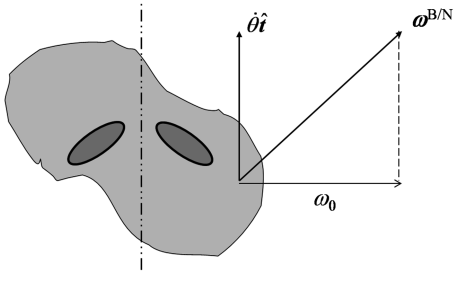

Fig. 10 Transverse rate.

Because the CMG-driven robot link's angular momentum is not conserved about $\hat{t}$, only the case in which $\boldsymbol{H}_c = 0$ at $t = 0$ is considered. The rotor momentum is determined by approximating the system momentum about the joint axis at maximum body rate using

$$\boldsymbol{H}_c|_{\dot{\theta}=\dot{\theta}_{\max}} \approx \boldsymbol{H}_c|_{t=0} + \left[\frac{\mathrm{d}\boldsymbol{H}_c}{\mathrm{d}t} \cdot t\right]_{\max} \tag{52}$$

The term in brackets is evaluated at $t = 0$ and $\Delta t/2$ to determine its maximum value. From the link's angular momentum in Eq. (19) and zero initial momentum, combined with the change in momentum about the joint axis from Eq. (29), the rotor momentum h_r is found by solving

$$\begin{aligned} &\boldsymbol{I}_b \cdot \boldsymbol{\omega}^{B/N}_{\max} \cdot \hat{\boldsymbol{t}} + 2h_r \sin\phi_{\max} \approx 0 \\ &\quad - [\boldsymbol{\omega}^{B/N} \times (\boldsymbol{I}_b \cdot \boldsymbol{\omega}^{B/N}) \cdot \hat{\boldsymbol{t}}]_{\max} \cdot \Delta t/2 \end{aligned} \tag{53}$$

The maximum gimbal angle used to calculate h_r is 70 deg (1.22 rad). Although h_r is determined from a fixed value of $\phi_{\max}$, the actual $\phi_{\max}$ achieved during the simulation varies. The range of $\phi_{\max}$ values reported in Table 1 reflects that Eq. (53) is an approximation. The ratio of energy used by CMGs to joint motors is shown for 1000 simulations in Fig. 11. We conclude that transverse rate does not significantly affect the energy used by a scissored pair if the rotor momentum is appropriately sized.

These first sections demonstrate that internal momentum exchange via CMGs can be designed to use the same amount of power as joint motors. The CMG system does add complexity and rotor losses associated with storing momentum when compared with the joint-motor-actuated robotic system. Undersized CMGs and bulky gimbals also add to the energy costs, but transverse-axis rotation does not. Correctly and accurately sizing the momentum requires knowledge of the bounds on link kinematics.

IV. Multilink Robot

The single-link robot arm with CMG actuation provides insight into the power and energy used by CMGs as a single unit. A multilink robot may gain additional benefits with CMGs, because the reactionless actuation affects not only the torques reacted onto the base but also torque reacted between links. The equations of motion for a three-link robot with scissored-pair CMG actuation have been derived by Carpenter and Peck [11]. They used Kane's equations as described in [28], equivalent to the principle of virtual power in this formulation [29], to derive the equations of motion. We extend their analysis to n-link robotic systems to compare joint motor or scissored-pair CMG actuation. Kane's equations may be written as [29]

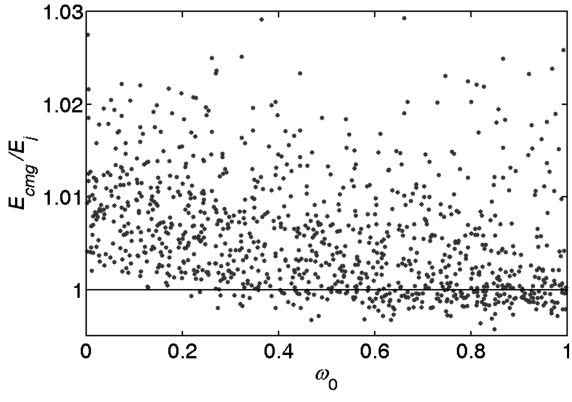

Fig. 11 Energy ratio plotted against transverse rate.

$$\sum_{i=1}^{n}(m_i \overset{N}{\dot{\boldsymbol{v}}}_i - \boldsymbol{F}_i^a)\cdot\frac{\partial \boldsymbol{v}_i}{\partial \dot{q}_k} + \sum_{i=1}^{n}(\overset{N}{\dot{\boldsymbol{H}}}_i - \boldsymbol{M}_i^a)\cdot\frac{\partial \boldsymbol{\omega}^{Bi/N}}{\partial \dot{q}_k} = 0 \quad \text{for } k = 1,\ldots,n \tag{54}$$

The number of links is n, i sums over each link, and k indexes the generalized coordinates. There are n generalized coordinates for a grounded serial linkage with revolute joints. The applied forces and moments on the ith link are $\boldsymbol{F}_i^a$ and $\boldsymbol{M}_i^a$; the superscript a distinguishes them from constraint forces and moments. The partial derivatives in Eq. (54) are known as partial velocities and indicate the component of the velocity or angular rate aligned with the appropriate generalized velocity. The velocities and rates are taken with respect to an inertial frame. Each body frame is denoted as Bi, with the basis vector $\hat{\boldsymbol{t}}_i$ aligned with the ith joint axis. The zeroth link is the nonrotating N frame. The angle of rotation of each link about its joint axis, θ_i, is the ith generalized coordinate q_i.

Recursive expressions for each term allow additional links to be added using the same block of code with another joint-angle command. Because this analysis uses prescribed motion, the expressions include no feedback terms. Including feedback requires an expression for the mass matrix, an exercise in algebra, and indexing (not included here). A schematic of the code structure for the joint motor simulation is shown in Fig. 12.

A. Joint Motor Actuation

The motion of the robot links is identical for both the joint-motor-driven and CMG-driven robots. The angular velocity of the ith link with respect to the Newtonian frame is defined recursively as

$$\boldsymbol{\omega}^{B/N} = \dot{q}_i\hat{\boldsymbol{t}}_i + \boldsymbol{\omega}^{Bi-1/N} \tag{55}$$

The angular acceleration is also given recursively:

$$\overset{N}{\boldsymbol{\omega}}{}^{Bi/N} = \ddot{q}_i\hat{\boldsymbol{t}}_i \times \boldsymbol{\omega}^{Bi-1/N} + \overset{N}{\boldsymbol{\omega}}{}^{Bi-1/N} \tag{56}$$

The angular velocity and acceleration of each link are calculated first because the other terms in Eq. (54) may be written in terms of these quantities. From Eq. (55), the partial angular velocity term in Eqs. (54) may be concisely written as

$$\frac{\partial \boldsymbol{\omega}^{Bi/N}}{\partial \dot{q}_k} = \begin{cases} \hat{\boldsymbol{t}}_k & k \le i \\ 0 & k > i \end{cases} \tag{57}$$

The subscript b is omitted for ease of notation. The angular momentum of link i and its derivative are given in Eqs. (14) and (15). Letting $\boldsymbol{I}_i$ denote $\boldsymbol{I}_b$ for link i and its actuator, $\overset{N}{\dot{\boldsymbol{H}}}_{j,i}$ is

$$\overset{N}{\dot{\boldsymbol{H}}}_{j,i} = \boldsymbol{I}_i\overset{N}{\dot{\boldsymbol{\omega}}}{}^{Bi/N} + \boldsymbol{\omega}^{Bi/N}\times\boldsymbol{I}_i\boldsymbol{\omega}^{Bi/N} \tag{58}$$

The applied moments on link i from the joint motors are

$$\boldsymbol{M}_{j,i}^a = \tau_{j,i}\hat{\boldsymbol{t}}_i - \tau_{j,i+1}\hat{\boldsymbol{t}}_{i+1} \tag{59}$$

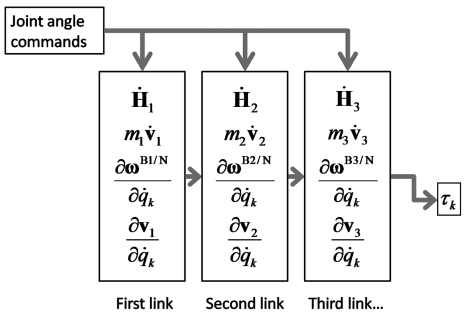

Fig. 12 Code structure for n-link robot with joint motors showing recursive dependence.

The applied moments become much less cumbersome after summing over all the links. The kth equation from Eq. (54) has a single torque term after taking the sum of applied moments projected onto the space of partial angular velocities:

$$\sum_{i=1}^{N}\boldsymbol{M}_{j,i}^a\cdot\frac{\partial\boldsymbol{\omega}^{Bi/N}}{\partial\dot{q}_k} = \sum_{i=k}^{N}\{(\tau_{j,i}\hat{\boldsymbol{t}}_i - \tau_{j,i+1}\hat{\boldsymbol{t}}_{i+1})\cdot\hat{\boldsymbol{t}}_k\} \tag{60}$$

$$\sum_{i=1}^{N}\boldsymbol{M}_{j,i}^a\cdot\frac{\partial\boldsymbol{\omega}^{Bi/N}}{\partial\dot{q}_k} = \tau_{j,k} \tag{61}$$

The dynamics due to the acceleration of the centers of mass of each link are not addressed in the single-link analysis. The first sum in Eq. (54) includes such dynamics. In a single link, these effects can be included by augmenting the inertia matrix in the equations of motion. The geometry of the robot is defined as follows. Let $\boldsymbol{l}_i$ be the vector from the i-frame origin to the $(i+1)$-frame origin, and let $\boldsymbol{r}_i$ be the vector from the i-frame origin to the center of mass of the link. The position $\boldsymbol{R}_i$ and velocity $\boldsymbol{v}_i$ of the ith link relative to the inertial frame origin are written recursively as

$$\boldsymbol{R}_i = \sum_{m=1}^{i-1}\boldsymbol{l}_m + \boldsymbol{r}_i \tag{62}$$

$$\boldsymbol{v}_i = \overset{N}{\dot{\boldsymbol{R}}}_i = \sum_{m=1}^{i-1}\boldsymbol{\omega}^{Bm/N}\times\boldsymbol{l}_m + \boldsymbol{\omega}^{Bi/N}\times\boldsymbol{r}_i \tag{63}$$

The acceleration of link i is

$$\overset{N}{\dot{\boldsymbol{v}}}_i = \sum_{m=1}^{i-1}\{\overset{N}{\dot{\boldsymbol{\omega}}}{}^{Bm/N}\times\boldsymbol{l}_m + \boldsymbol{\omega}^{Bm/N}\times(\boldsymbol{\omega}^{Bm/N}\times\boldsymbol{l}_m)\} + \overset{N}{\dot{\boldsymbol{\omega}}}{}^{Bi/N}\times\boldsymbol{r}_i + \boldsymbol{\omega}^{Bi/N}\times(\boldsymbol{\omega}^{Bi/N}\times\boldsymbol{r}_i) \tag{64}$$

The corresponding partial velocities are

$$\frac{\partial\boldsymbol{v}_i}{\partial\dot{q}_k} = \begin{cases} \hat{\boldsymbol{t}}_k\times\left(\boldsymbol{r}_i + \sum_{\substack{m=k\\k\neq i}}^{i-1}\boldsymbol{l}_m\right) & i \ge k \\ 0 & i < k \end{cases} \tag{65}$$

With no applied forces in the problem, $\boldsymbol{F}^a = 0$.

B. CMG-Actuated System

As is the case for the single-link equations, the equations for the multibody CMG-driven robot arm share most of the terms from the equations for the joint-motor-driven robot arm. The only difference is that there are no applied joint torques (i.e., the gimbal motor is considered an internal force) and

$$\sum_{i=1}^{N}\boldsymbol{M}_i^a\cdot\frac{\partial^{\boldsymbol{\omega}^{Bi/N}}}{\partial\dot{q}_k} = 0 \tag{66}$$

Instead, motion is controlled with internal angular momentum from the CMGs. The angular momentum of a link and its CMGs is given by Eq. (19). The angular momentum derivative given by Eq. (20) for a single link takes the same form for the ith link:

$$\overset{N}{\dot{\boldsymbol{H}}}_{c,i} = \boldsymbol{I}_i\overset{N}{\dot{\boldsymbol{\omega}}}{}^{Bi/N} + \overset{N}{\dot{\boldsymbol{\omega}}}{}^{Bi/N}\times\boldsymbol{I}_i\overset{N}{\boldsymbol{\omega}}{}^{Bi/N} + 2h_{r,i}\dot{\phi}_i\cos\phi_i\hat{\boldsymbol{t}}_i + \overset{N}{\boldsymbol{\omega}}{}^{Bi/N}\times 2h_{r,i}\sin\phi_i\hat{\boldsymbol{t}}_i \tag{67}$$

This equation is projected onto the partial velocities in Eq. (57). The equations of motion for the CMG-actuated robot are related to the equations of motion for the joint-motor-driven robot by the following:

$$\sum_{i=1}^{n} \boldsymbol{H}_{c,i}^{N} \cdot \frac{\partial \boldsymbol{\omega}^{Bi/N}}{\partial \dot{q}_k} = \sum_{i=1}^{n} \boldsymbol{H}_{j,i}^{N} \cdot \frac{\partial \boldsymbol{\omega}^{Bi/N}}{\partial \dot{q}_k} + 2h_r \dot{\phi}_i \cos\phi_i \hat{\boldsymbol{t}}_i \cdot \hat{\boldsymbol{t}}_k + \boldsymbol{\omega}^{Bi/N} \cdot (2h_r \sin\phi_i \hat{\boldsymbol{t}}_i \times \hat{\boldsymbol{t}}_k) \quad \text{for } k \le i \tag{68}$$

The equations of motion for the joint-motor-driven robot can be assembled into the following form with a mass matrix M and the velocity product terms V [29]:

$$M(\Theta, \dot{\Theta})\ddot{\Theta} + V(\Theta, \dot{\Theta}) = T \tag{69}$$

The n joint angles, rates, and accelerations and the joint torques are the elements of the arrays Θ, $\dot{\Theta}$, $\ddot{\Theta}$, and T. The same left-hand side of this equation can be used to express the motion of a CMG-driven robot. Including the gimbal dynamics results in a differential equation in both joint angles Θ and the gimbal angles Φ,

$$M(\Theta, \dot{\Theta})\ddot{\Theta} + V(\Theta, \dot{\Theta}) = -B(\Theta, \dot{\Theta}, \Phi) - D(\Theta, \Phi)\dot{\Phi} \tag{70}$$

The matrix D is an upper-triangular matrix that reflects the alignment of an outboard scissored pair with the inboard link of interest. In other words, once T has been determined for an equivalent system, the gimbal trajectories may be determined by

$$T = -B(\Theta, \dot{\Theta}, \Phi) - D(\Theta, \Phi)\dot{\Phi} \tag{71}$$

The Φ are then used with Eq. (11) to find the gimbal torques. Implementation of a CMG-robot control scheme could consist of a standard control algorithm for T and a nested control algorithm for Φ.

V. Two-Link Robot

The two-link robot gives insight into the design considerations for multilink robots by illustrating the effect of neighboring joints on a

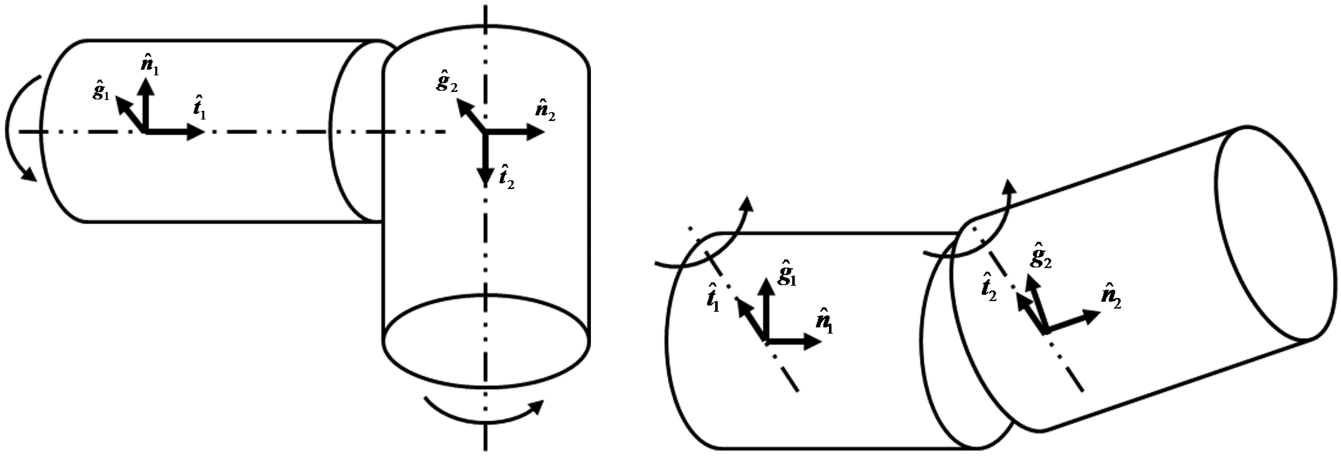

a) b)

Fig. 13 Joint topologies: a) orthogonal joint axes and b) parallel joint axes.

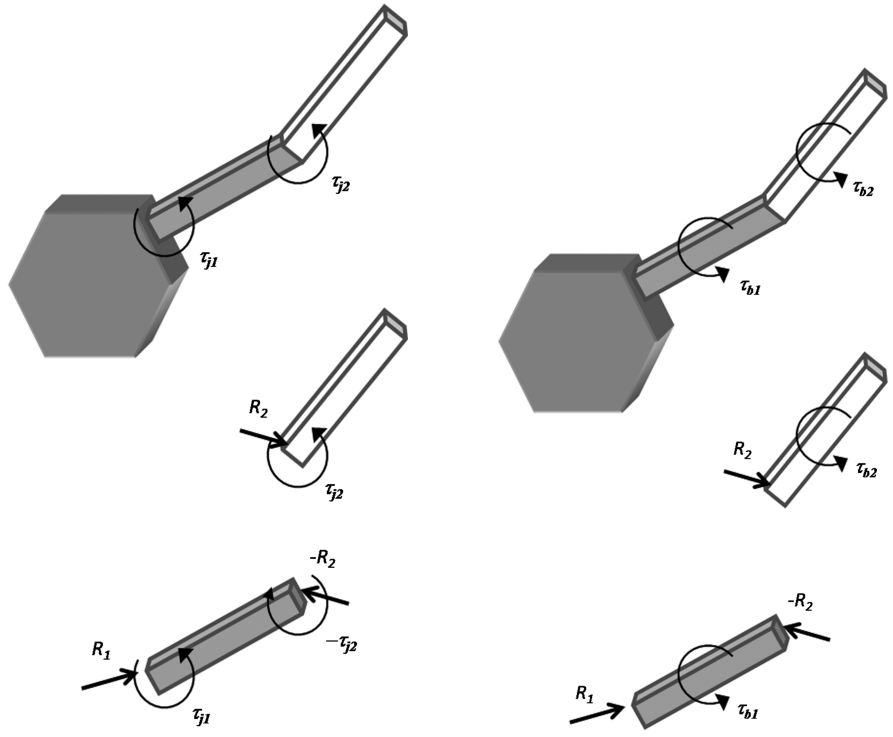

a) b)

Fig. 14 Free-body diagram of a two-link robot: a) joint torque and b) body torque.

Table 2 Parameter value ranges for two-link simulations

	Parameters			Monte Carlo inputs			
	I_{cmg}, kg · m^2	h_r, N.m.s	$I_{b,\hat{t}}$ kg · m^2	$r_i(\cdot)$, m	$l_1(\cdot)$, m	Δt_0, s	sign($\Delta\theta$)
Ortho	0.1	0.53	0.8–1.2	−0.5–0.5	−1–1	0–4	±
Parallel	0.1	0.53	0.8–1.2	−0.5–0.5	−1–1	0–4	±

given link based on whether joint torques or CMGs are used. First, the applied CMG torques are replaced by body torques. This idealized system shows a difference in power consumed by CMGs and joint motors that is not seen in the single-link example. Simulations further highlight the power difference for different robotic motions, including some that are particularly well suited for CMGs.

A. Body-Torque Analogy

With joint motor actuation, each motor moves its own link and reacts the torques produced by links further down the chain according to the angles between the joint axes: the joint topology. Two distinct joint topologies for a two-link robot are the planar robot with parallel joint axes and a pitch-roll robot with orthogonal joint axes, shown in Fig. 13. The key difference between these two topologies is that a torque about the second joint of the pitch-roll robot is perpendicular to the first joint axis and will be transmitted to the base via a constraint torque. Torque about the second joint of a planar robot is coupled to the first joint, as shown in the free-body diagram of a two-link robot with joint torques (Fig. 14). A subscript j or b denotes joint torques and body torques. Figure 14 also shows that, as with CMGs, a body torque must have zero torque about the joint axis.

The equations of motion in matrix form with joint torques are already given in Eq. (69). For the case of body torques, let $\gamma_{i,m}$ be the dot product of the two joint axes:

$$\gamma_{i,m} = \hat{\boldsymbol{t}}_i \cdot \hat{\boldsymbol{t}}_m \tag{72}$$

The equations of motion for the body torques T_b can be written with a vector of body torques:

$$M(\Theta, \dot{\Theta})\ddot{\Theta} + V(\Theta, \dot{\Theta}) = \begin{bmatrix} 1 & \gamma_{1,2} \\ 0 & 1 \end{bmatrix} T_b \tag{73}$$

The matrix D in Eq. (70) is also an upper-triangular matrix with the $\gamma_{i,m}$ multiplied by $2h_r \cos\phi_i$. Equations (69) and (73) relate body torques to joint torques:

$$T_b = \begin{bmatrix} 1 & -\gamma_{1,2} \\ 0 & 1 \end{bmatrix} T_j \tag{74}$$

The free-body diagram of the planar two-link robot in Fig. 14 shows that the body torque on the first link is the difference of the two joint torques, in agreement with (74).

The torque relationship does not conclude the question of joint-vs-body torques. The angular velocity required to determine the power needed by each actuator also varies. Joint torques are applied along the joint velocities: the $\dot{\theta}$ used to describe the motion of the robot. The body torques are applied relative to the inertial frame. Therefore, power is determined from the component of the vector $\boldsymbol{\omega}^{Bi/N}$ along the joint axis, determined by summing up the inboard joint velocities scaled by $\gamma_{i,m}$. The body velocities in terms of the joint velocities for the two-link case are

$$\Theta_b = \begin{bmatrix} 1 & 0 \\ \gamma_{1,2} & 1 \end{bmatrix} \Theta_j \tag{75}$$

The power of the body torques can now be easily expressed in terms of the joint torques and velocities. For a perfectly lossless system (e.g., with only springs), the product of torques and velocities is equal in both cases. As discussed previously, this study assumes a nonconservative system. Power required by torque applied directly to the body can be written in terms of the equivalent joint torque and joint velocity:

$$|P_{b1}| + |P_{b2}| = |\dot{\theta}_{j1}\tau_{j1} - \gamma_{1,2}\dot{\theta}_{j1}\tau_{j2}| + |\gamma_{1,2}\dot{\theta}_{j1}\tau_{j2} + \dot{\theta}_{j2}\tau_{j2}| \tag{76}$$

Once again, without the absolute values, this expression would reduce to the power for the joint torques. This expression shows that joint torques and body torques have different power requirements and energy demands for certain maneuvers. The single-link analysis shows that CMGs are an excellent means of body-torque actuation and may be used to exploit the differences between body torques and joint torques. Replacing CMGs with body torques also simplifies the design of a multilink robot that uses CMGs.

B. Two-Link Simulations

We contrast a robot with orthogonal joint axes and a robot with parallel joint axes as two possible joint topologies for a two-link robot. For example, the first provides orientation control with two degrees of freedom (e.g., azimuth and elevation) for pointing a sensor at a target. The latter provides range for reaching tasks for a manipulation robot on a spacecraft. These two cases represent two extremes of the potential differences between body torques and joint torques, as shown in Eq. (76) with the dot product of the torque-output-direction vectors $\gamma_{1,2}$ equal to 0 or 1 [Eq. (72)].

1. *Link Rate and CMG Size*

For both joint topologies, the mass properties and motion of the outer link affect CMG sizing through the system angular momentum. The net angular velocity of the outer link includes a component from the first joint that can project along the second joint axis, because the joint axes are not necessarily principal axes of inertia. Therefore, sizing the CMGs on a two-link robot requires careful bookkeeping of a time-varying inertia and angular velocities of the links. The CMGs on a multilink robot could be sized according to the expected maximum angular momentum about each joint. An economic alternative used in these simulations is to place identical CMGs on each link and adjust the maximum joint velocity so that the net angular momentum is bounded by the capacity of the CMGs. The maximum angular velocities that do not saturate the CMGs are determined using an expanded version of the approximate change in momentum about the joint axis from Eq. (53). The angular momentum about each joint axis depends on the rate about both axes, yielding a system of two equations that is quadratic in the joint velocities.

For this exploratory study, the maximum acceleration and jerk are arbitrarily set to the same numerical value as the adjusted maximum angular velocity to satisfy Eq. (47). The angle of rotation and slew duration are given by Eqs. (48) and (49). The start time of the rotations is offset by Δt_0, with either joint randomly assigned to move first. The parameters used for a 1000-trial simulation are given

Table 3 Range of results for two-link simulations

	Intermediate calculations				Result
	ω_{max}, s^{-1}	I_{max}, kg · m^2	ϕ_{max}, deg	$\Delta\theta$, deg	E_{cmg}/E_j
Ortho	0.1–0.5	1.9–6.1	7–74	10–59	1–1.33
	0.6–1.2	0.8–1.6	50–80	65–134	——
Parallel	0.03–1.0	1.0–4.0	3–73	4–112	−0.49–1.38
	0.0–0.9	0.9–1.5	1–73	0.2–98	——

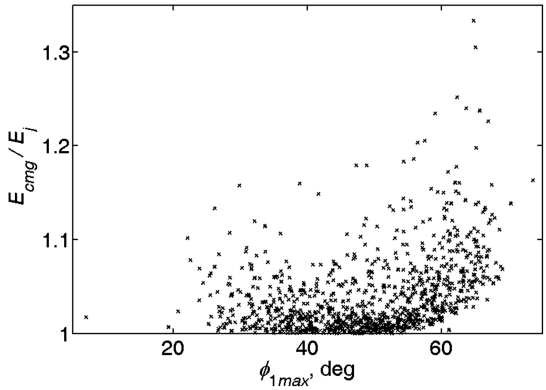

Fig. 15 Performance of CMGs on robot arm with orthogonal joint axes.

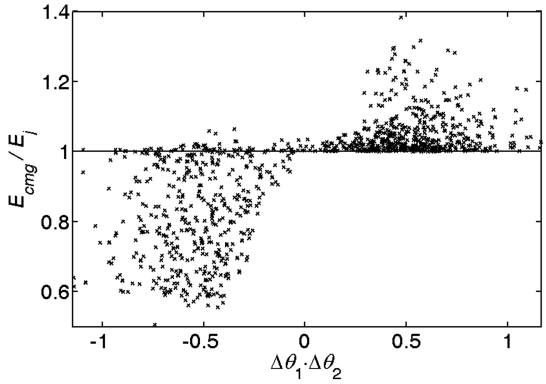

Fig. 16 Joint-angle command product as an indicator of performance for parallel joint axes.

in Table 2. The principal inertias, center-of-mass offset, and joint-axis locations are randomly assigned componentwise from a uniform distribution over the range given in Table 3. The uniform distribution is merely meant to provide a qualitative assessment, not to encourage statistical inferences from the outputs. The maximum inertia about the joint axis, the maximum body rate, and maximum gimbal angle are calculated from the assigned parameters. Table 3 gives ranges for these values.

Table 4 Summary of design tool

Description	Reference in text
Calculate CMG dynamics from equivalent joint motor robot	Eq. (71)
Conservation of angular momentum about joint axis	Eq. (29)
Gimbal-rate bound	Eq. (32)
Torque amplification	Eq. (36)
Gimbal-torque-limited design	Eqs. (39) and (40)
Gimbal acceleration and robot jerk	Eq. (41)
Relative power costs of CMGs to joint motors	Eq. (45)

2. Orthogonal Joint Axes

The equations of motion are decoupled under the following conditions: if the joint axes are orthogonal, if the outer link is axisymmetric about its joint axis, and if the two joint axes intersect. These conditions also satisfy conservation of momentum about the joint axes stated in Eqs. (27–29), adjusted for the two-link robot. In such a case, the power performance is calculated as for two independent single links. These simulations specifically offset the joint axes, translate the centers of mass, and include offdiagonal terms in the inertia matrices to avoid repeating the results in the earlier section.

Figure 15 is a plot of the energy ratio for the two-link system as a function of the maximum gimbal angle of the inner link, $\phi_{1\,\max}$. The greater inertia about the first joint axis causes the inner link's gimbal angle to influence the energy ratio more than the outer link's gimbal angle, as shown in Fig. 15. The effect of the combined inertia of the links about the first joint axis is included in $\phi_{1\,\max}$ through Eq. (53). As with the single-link robot, the energy ratio is greater than zero, with some dependence on the size of the CMG, as represented by the maximum angle for the first gimbal. However, some trials in this simulation are not very power-efficient, due to increased inertia about the joint axes without a corresponding decrease in the other terms of the relative power in Eq. (45).

3. Parallel Joint Axes

None of the simulations thus far have indicated that CMGs offer an advantage in terms of power and energy over joint motors, although the analysis of body torques vs joint torques in Sec. V.A suggests that such an advantage may exist. In these simulations, identical CMGs are again used on each link and the maximum joint rate is adjusted in accordance with the momentum capability of the scissored pair. For parallel joint axes, the sign of each joint's rotation is critical in determining the maximum joint rate. When both joints move together, the outer link saturates its CMGs more easily, because both joint velocities add to determine the link's angular velocity with respect to ground. When the joints move in opposite directions, the outer link can attain a high joint rate while keeping the angular momentum low. The maximum joint velocities are determined from the CMG momentum by taking the individual joint velocity if they are of opposite sign or the sum of the two if they share the same sign. Zero velocity of either link is possible due to the start-time offset Δt_0.

For 1000 trials over the same range of parameters as the orthogonal-axes case, the energy ratio is less than zero for 403 trials. Figure 16 shows the values of the energy ratio plotted against the sign of the product of the joint-angle commands. The results show that CMGs are more efficient than joint motors when the joints move in opposite directions, as they must for reaching tasks. Joint motors represent a more power-efficient choice when the joints move together (e.g., overhand throwing motions).

VI. Discussion

Throughout this paper, a number of design aids and pros and cons of CMG-driven robots have been discussed. Results that relate to the design of a CMG system are summarized in Table 4. The torque amplification and gimbal-torque-limited CMG sizing were obtained through a general treatment of the CMG size, allowing for the possibility of rapid robot-arm movement beyond motions typical of single-body spacecraft, because a link in a robot arm may have a

Table 5 Pros and cons of CMG-driven robotic joints

Pros	Cons
Reduces reaction forces on spacecraft	Adds mechanical complexity
Simplifies spacecraft attitude and robot control interactions	Sensitive to conservation of angular momentum about each joint axis (but robust to transverse rates otherwise)
Uses existing dynamics and control methods from robotics with a nested loop for the CMGs	Spin-up and quiescent power costs
Theoretical power performance near that of joint motors, better for reaching motions	Vibration from spinning rotors
CMG dynamics limit jerk of robot	Unable to provide persistent torques

much smaller inertia relative to the CMG inertia than for a spacecraft with additional systems attached to the same bus.

A summary of the pros and cons of a CMG robot as discussed in this paper and related references are provided in Table 5. Although a treatment of a hybrid actuation system is beyond the scope of this paper, Table 5 indicates the utility of combining CMGs and joint motors. Strategically placed CMGs on the robot could reduce reaction forces on the spacecraft by reducing the joint torques. Joint motors in turn would provide a path to exchange momentum between robot links and the spacecraft to restore the CMGs to a neutral position, relaxing the requirement that angular momentum be conserved about each joint axis. Joint motors also provide a means to produce or resist persistent torques that would otherwise saturate the CMGs. An operations concept for a combined actuation method is to use the CMGs for positioning the robot and payload into an anchored position on the spacecraft and to let the joint motors provide the torque for any operations once the payload is anchored.

VII. Conclusions

In the limit of an ideal rotor, momentum actuation via control moment gyroscopes (CMGs) is theoretically as efficient as rigid-body actuation via joint motors (i.e., there is no hidden cost to using momentum actuation comparable with thermodynamics' second law for dynamics). Friction losses and electromagnetic inefficiencies represent additional power costs in physical CMGs. A CMG-driven robot reduces the attitude control effort required to respond to robot motions by distributing the attitude control among the robot joints and helps simplify the dynamic interactions between the spacecraft and robot. Although the complexity of CMGs does not warrant replacing joint motors purely for power savings, the additional benefits of eliminating a reaction torque on a spacecraft cannot be ignored.

Acknowledgments

D. Brown was supported by the National Science Foundation grant number 0333366 for the Cornell Integrative Graduate Education and Research Traineeship (IGERT) Program in Nonlinear Systems. The authors thank M. Carpenter and I. Livingston for discussions on reactionless actuation.

References

[1] Lappas, V., Steyn, W. H., and Underwood, C., "Design and Testing of a Control Moment Gyroscope Cluster for Small Satellites," *Journal of Spacecraft and Rockets*, Vol. 42, No. 4, 2005, p. 729. doi:10.2514/1.7308

[2] Lappas, V. J., Steyn, W. H., and Underwood, C. I., "Attitude Control for Small Satellites Using Control Moment Gyros," *Acta Astronautica*, Vol. 51, Nos. 1–9, 2002, pp. 101–111. doi:10.1016/S0094-5765(02)00089-9

[3] Wie, B., Bailey, D., and Heiberg, C., "Rapid Multitarget Acquisition and Pointing Control of Agile Spacecraft," *Journal of Guidance, Control, and Dynamics*, Vol. 25, No. 1, 2002, pp. 96–104. doi:10.2514/2.4854

[4] Carpenter, M. D., "Dynamics and Control of Gyroscopically Actuated Space-Robotic Systems," Ph. D. Dissertation, Dept. of Theoretical and Applied Mechanics, Cornell Univ., Ithaca, NY, 2009, pp. 49–81.

[5] Murray, R. M., Li, Z., and Sastry, S., *A Mathematical Introduction to Robotic Manipulation*, CRC Press, Boca Raton, FL, 1994, pp. 190–198.

[6] Craig, J. J., *1955—Introduction to Robotics: Mechanics and Control*," Pearson Education, Upper Saddle River, NJ, 2005, p. 400.

[7] Longman, R. W., Lindberg, R. E., and Zedd, M. F., "Satellite-Mounted Robot Manipulators--New Kinematics and Reaction Moment Compensation," *International Journal of Robotics Research*, Vol. 6, No. 3, 1987, pp. 87–103. doi:10.1177/027836498700600306

[8] Nakamura, Y., and Mukherjee, R., "Nonholonomic Path Planning of Space Robots via a Bidirectional Approach," *IEEE Transactions on Robotics and Automation*, Vol. 7, No. 4, 1991, pp. 500–514. doi:10.1109/70.86080

[9] Moosavian, S. A. A., and Papadopoulos, E., "Free-Flying Robots in Space: An Overview of Dynamics Modeling, Planning and Control," *Robotica*, Vol. 25, No. 05, 2007, pp. 537–547. doi:10.1017/S0263574707003438

[10] Billing-Ross, J. A., and Wilson, J. F., "Pointing System Design for Low-Disturbance Performance," *AIAA Guidance, Navigation, and Control Conference*, CP4106, Vol. 1, AIAA, Washington, D.C., 1988, pp. 444–451.

[11] Carpenter, M. D., and Peck, M. A., "Dynamics of a High-Agility, Low-Power Imaging Payload," *IEEE Transactions on Robotics and Automation*, Vol. 24, No. 3, 2008, pp. 666–675. doi:10.1109/TRO.2008.924264

[12] Osuka, K., Yoshida, K., and Ono, T., "New Design Concept of Space Manipulator: A Proposal of Torque-Unit Manipulator," *33rd IEEE Conference on Decision and Control*, Vol. 2, Inst. of Electrical and Electronics Engineers, New York, 1994, pp. 1823–1825. doi:10.1109/CDC.1994.411118

[13] Romano, M., and Agrawal, B. N., "Attitude Dynamics/Control of Dual-Body Spacecraft with Variable-Speed Control Moment Gyros," *Journal of Guidance, Control, and Dynamics*, Vol. 27, No. 4, 2004, pp. 513–525. doi:10.2514/1.2564

[14] Yang, L. F., Mikulas, M. M., Jr., and Park, K. C., "Slewing Maneuvers and Vibration Control of Space Structures by Feedforward/Feedback Moment-Gyro Controls," *Journal of Dynamic Systems, Measurement, and Control*, Vol. 117, 1995, pp. 343–351. doi:10.1115/1.2799125

[15] Schaub, H., Vadali, S. R., and Junkins, J. L., "Feedback Control Law for Variable Speed Control Moment Gyros," *Journal of the Astronautical Sciences*, Vol. 46, No. 3, 1998, pp. 307–328.

[16] Koh, S. K., Ostrowski, J. P., and Ananthasuresh, G. K., "Control of Micro-Satellite Orientation Using Bounded-Input, Fully-Reversed MEMS Actuators," *International Journal of Robotics Research*, Vol. 21, Nos. 5–6, 2002, p. 591. doi:10.1177/027836402761393388

[17] Van Riper, R. V., and Liden, S. P., "A New Fail Operational Control Moment Gyro Configuration," *AIAA Guidance, Control, and Flight Mechanics Conference*, AIAA, Washington, D.C., 1971, pp. 71–936.

[18] Schaub, H., and Junkins, J. L., *Analytical Mechanics of Space Systems*, AIAA, Reston, VA, 2003, pp. 438–440.

[19] Liden, S. P., "Precision CMG Control for High-Accuracy Pointing," *Journal of Spacecraft and Rockets*, Vol. 11, 1974, p. 236. doi:10.2514/3.62049

[20] Kurokawa, H., "Survey of Theory and Steering Laws of Single-Gimbal Control Moment Gyros," *Journal of Guidance, Control, and Dynamics*, Vol. 30, No. 5, 2007, p. 1331. doi:10.2514/1.27316

[21] Margulies, G., and Aubrun, J. N., "Geometric Theory of Single-Gimbal Control Moment Gyro Systems," *Journal of the Astronautical Sciences*, Vol. 26, No. 2, 1978, pp. 159–191.

[22] Havill, J. R., and Ratcliff, J. W., "A Twin-Gyro Attitude Control System for Space Vehicles," NASA TN D-2419, 1964.

[23] Brown, D., and Peck, M. A., "Scissored Pair Control Moment Gyros: A Mechanical Constraint Saves Power," *Journal of Guidance, Control, and Dynamics*, Vol. 31, No. 6, 2008, pp. 1823–1826. doi:10.2514/1.37723

[24] Liska, D., "A Two-Degree-of-Freedom Control Moment Gyro for High-Accuracy Attitude Control," *Journal of Spacecraft and Rockets*, Vol. 5, No. 1, 1968, pp. 74–83. doi:10.2514/3.29188

[25] Oh, H. S., Vadali, S. R., and Junkins, J. L., "Use of the Work-Energy Rate Principle for Designing Feedback Control Laws," *Journal of Guidance, Control, and Dynamics*, Vol. 15, No. 1, 1992, pp. 275–277. doi:10.2514/3.20831

[26] Lappas, V. J., Steyn, W. H., and Underwood, C. I., "Torque Amplification of Control Moment Gyros," *Electronics Letters*, Vol. 38, No. 15, 2002, pp. 837–839. doi:10.1049/el:20020590

[27] Peck, M. A., "Uncertainty Models for Physically Realizable Inertia Dyadics," *Journal of the Astronautical Sciences*, Vol. 54, No. 1, 2006, pp. 1–16.

[28] Kane, T. R., and Levinson, D. A., *Dynamics: Theory and Applications*, McGraw–Hill, New York, 1985, p. 158.

[29] Moon, F. C., "Applied Dynamics: With Applications to Multibody and Mechatronic Systems," Wiley, New York, 1998, pp. 269–271.